Applied Mathematical Modelling 77 (2020) 1331–1347

Contents lists available at ScienceDirect

Applied Mathematical Modelling

journal homepage: www.elsevier.com/locate/apm

Numerical simulation of flow-induced vibration of two cylinders elastically mounted in tandem by immersed moving boundary method

G.F. Narváez [a,*], E.B. Schettini [a], J.H. Silvestrini [b]

[a] Instituto de Pesquisas Hidráulicas (IPH), Universidade Federal do Rio Grande do Sul, Porto Alegre, RS, Brazil
[b] Escola Politécnica, Pontifícia Universidade Católica do Rio Grande do Sul, Porto Alegre, RS, Brazil

ARTICLE INFO

Article history:
Received 24 October 2018
Revised 25 July 2019
Accepted 3 September 2019
Available online 10 September 2019

Keywords:
Numerical simulation
Immersed boundary method
Flow-induced vibration
Tandem cylinders

ABSTRACT

A numerical study is performed on flow-induced vibrations of two cylinders of diameter D, in tandem configuration relative to the free-stream uniform flow U at low Reynolds numbers $Re = UD/\nu$. In order to solve numerically the incompressible momentum and continuity equations, the in-house code `Incompact3D` is used. Compact sixth-order finite differences for spatial differentiation and second-order Adams–Bashforth scheme for time advancement are employed. The cylinders movement is modeled as a mass-damper-spring system which is solved by a fourth-order Runge–Kutta scheme. To represent the multiple moving cylinders in an immersed boundary method framework, a modification in the Poisson equation is proposed. The modified algorithm was evaluated and applied for scenarios with zero, one and two translational degrees of freedom to oscillate. The validation is carried out against several numerical and experimental previous works. The results are analyzed in terms of the forces on cylinders, Strouhal number of the wake, streamwise velocity profiles and cylinders oscillation amplitudes and frequencies. The algorithm could satisfactorily represent the resonance and wake-flutter phenomena. In the most cases, the rear cylinder has greater oscillations than the front cylinder. However, a state was identified where the cross-stream oscillation amplitudes of the front cylinder are lower than those of the rear cylinder. In this state, the lift force acts as negative spring on the front cylinder (amplifying its oscillations) and as a damper on the rear cylinder (controlling its oscillations). The scenarios with two degrees of freedom (*2dof*) have higher oscillation amplitudes than the equivalent scenarios with one degree of freedom. Moreover, the streamwise oscillation amplitudes are not negligible in relation to the cross-stream oscillation amplitudes. On the other hand, for *2dof*, when the Reynolds number increases the clashing risk also increases, since the cylinders proximity is narrowed.

1. Introduction

Several engineering and biological applications involve Fluid–Solid Dynamic Interaction (*FSI*). For instance, structures submitted to sea/river currents (e.g., bridge piers, risers and vegetation) and wind flux (e.g. buildings, electricity transmission

* Corresponding author.
E-mail addresses: gabriel.narvaez@ufrgs.br (G.F. Narváez), bcamano@iph.ufrgs.br (E.B. Schettini), jorgehs@pucrs.br (J.H. Silvestrini).

https://doi.org/10.1016/j.apm.2019.09.007
0307-904X/

lines, anchor cables, cable-stayed bridges) represent some common cases of *FSI*. Moreover, the complex nature of this non-linear interaction makes *FSI* challenging and interesting for scientific research. From the wide range of *FSI* phenomena, we focus on two types of Flow-induced vibration (*FIV*): Vortex-induced vibration (*VIV*) and Wake-induced vibration (*WIV*). *VIV* phenomenon is associated with the solid motion caused by forces induced by the vortex shedding (Williamson and Govardhan [1] make a comprehensive review on the topic). Assi et al. [2] define *WIV* as a fluid-elastic mechanism able to yield oscillations of a body immersed in the wake interference region behind a bluff body [3–5].

Cylinders arrays submitted to cross-flow (flow normal to main cylinder axis) can develop both *VIV* and *WIV* which, eventually, cause high oscillations amplitudes. Under certain conditions, the restitutive and damping forces of solid structures are not able to control the fluid forces, then self-excited oscillations could lead to structure failure. It should be pointed out that fluid-elastic instabilities, also referred to self-excited oscillations [6], of cylinders arrays submitted to cross-flow, were the cause of damages worldwide whose costs were estimated at 1000 M$ over one decade [7].

In-line cylinders arrays whose center-to-center line is parallel to the free-stream flow direction is defined as tandem cylinders arrangement [8,9]. For this configuration, separated flow on upstream cylinders forms free shear layers that interact with downstream cylinders surfaces. Thus, the behavior is substantially different from a single cylinder, and strongly influenced by the center-to-center spacing between the cylinders S, as observed in previous works [e.g., 10,11]. For two fixed tandem cylinders of same diameter D, it can be defined a *critical non-dimensional spacing* $(S/D)_c$ as the distance S/D associated to unstable reattachment of the upstream free shear layers on the downstream cylinder surface, i.e. the spacing for which the upstream wake is formed and developed inside the gap between cylinders. This critical spacing determines three flow patterns: (i) stable reattachment of upstream free shear layers on downstream cylinder ($S/D < (S/D)_c$), (ii) bistable reattachment ($S/D \approx (S/D)_c$) and (iii) vortex wake completely developed in the gap between the cylinders ($S/D > (S/D)_c$). Fluctuating and time-averaged force coefficients, fluctuating and time-average pressure on cylinders surfaces and the Strouhal number, as a function of S/D, show hysteretic discontinuities at $S/D \approx (S/D)_c$ [12]. At low Reynolds numbers ($Re = 100$ and $Re = 300$), Huhe et al. [13] observed that the critical spacing varies in the interval $3.5 < (S/D)_c < 4.5$, while, for $Re \sim 10^4$, Kiya et al. [14], Igarashi [3] and Alam et al. [12] identified $3 < (S/D)_c < 4$.

Depending on the temporal scale relation between solid and fluid oscillations, the *FIV*-modeling of rigid cylinders can be satisfactorily represented by *fixed, forced* or *elastically-mounted* cylinders. Here, a cylinder with one degree of freedom (*1dof*) can freely oscillate in cross-stream *or* streamwise direction, while, a cylinder with two degrees of freedom (*2dof*) oscillates in both directions.

There are several numerical [e.g., [15–17]] and experimental [e.g., 18,19] studies on flow around two *fixed* cylinders in a tandem arrangement, but comparatively few researches involving cylinders in tandem submitted to *FIV*. Some authors consider *fixed* upstream cylinder and *oscillating* downstream cylinder [e.g., [20–22]], and both *oscillating* cylinders with *1dof* or *2dof* [e.g., [16,17,23]]. However, it is not clearly understood the *FIV* of two cylinders in tandem configuration with *2dof* *each one* at initial spacing equal to the critical one (which is around $(S/D)_c \approx 3.5$, for fixed cylinders).

In some cases, flow around tandem arrays with *1dof* has less complexity and different solid dynamic response than the corresponding *2dof* system. For instance, in *1dof* system, the vibration control is applied by increasing the mechanical damping, while in a *2dof* system, increasing damping could yield higher energy absorption of the downstream cylinder and change the cylinder modal pattern [6]. For upstream fixed cylinder and flexible downstream cylinder, Huera-Huarte et al. [21] identified multi-mode vortex and wake-induced vibrations yielding higher amplitude response than a single oscillating cylinder in resonance. The resonance occurs in the so-called lock-in or synchronization interval. Lock-in is associated to the control of shedding process by the elastic structure, in a bandwidth around the fundamental frequency [24]; i. e. the vortex shedding frequency f is "locked" in the fundamental frequency f_N of structure oscillation ($f \approx f_N$).

From the above statements, the governing parameters for elastically-mounted smooth circular cylinders, initially in tandem arrangement, are: the Reynolds number Re; the reduced velocity U_R (which represents the relation between the solid and fluid time scales); the center-to-center spacing S/D; structural parameters as the mass-damping parameter $= m\zeta$ (where m is the reduced mass and ζ is the critical damping ratio), and the number of degrees of freedom (*dof*).

The numerical strategies to represent solid geometries can be classified as: *non-body conformal* methods (as the Immersed Boundary Method, *IBM*) which, basically, consider the body embedded in the grid, so the grid is not body shape dependent, in contrast to *body-conformal* methods. In high-order schemes framework, the *IBM* allows using a Cartesian grid, which allows straightforward implementation and accurate computations of the discrete operators (spatial derivatives) near the fluid–solid interface [25]. The *IBM* could make the moving boundaries representation simpler than the body-conformal methods, because the grid is not reformulated every body displacement. In this paper, the flow governing equations are numerically solved by using the high precision code `Incompact3D` [26], coupled with the Immersed Boundary Method (*IBM*) proposed by Parnaudeau et al. [27]. In this work, this *IBM* is extended in order to incorporate several moving cylinders. In Section 2 the governing equations and the numerical algorithm are presented and described.

This algorithm is evaluated for two cylinders fixed, in Galilean translation and in *1dof* Flow-induced vibration (Section 3). The consistent validation allowed applying the algorithm to simulate the *FIV* of two cylinders at low Reynolds numbers, aiming to analyze the dynamic cylinders responses and flow characteristics (Section 4). This is achieved by studying the *2dof* system in detail and comparing it with the *1dof* system, for Re equal to 200 and 300, U_R from 2 to 14, $m = 1$, $\zeta = 0.007$ and $S/D = (S/D)_c \approx 3.5$. This reduced velocity interval is especially interesting because galloping instability (or wake-induced flutter) and resonance phenomenon could simultaneously occur [28]. Finally, Section 5 is dedicated to present some concluding remarks as well as the main highlights of this study.

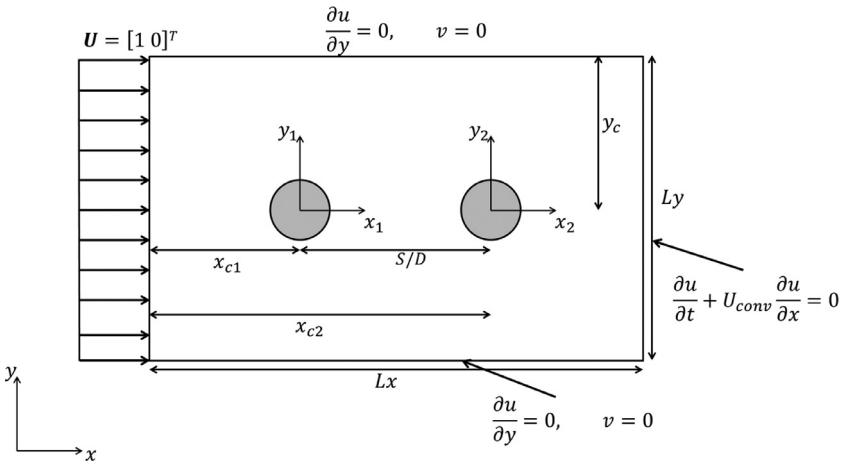

Fig. 1. Flow configuration, computational domain and boundary conditions, where $\mathbf{u} = [u\ v]^T$ and U_{conv} is the mean convection velocity of the main outflow structures.

2. Computational method

In this section, we present the governing equations, the boundary conditions and the numerical methodology. The governing equations are: the fluid mass and momentum balance equations, the solid dynamic equation and the control volume formulation to compute the fluid forces. It must be pointed out that here, the fluid and solid dynamic equations are online coupled to accurately represent the non-linear physical processes involved in Fluid–structure interaction. The numerical methodology, involves time advancement and the *IBM* formulation proposed to represent one or more moving cylinders. In the following analysis, all quantities are assumed to be scaled by the cylinder diameter, the free-stream velocity and the fluid density. As a consequence of the non-dimensionalization, the dimensionless diameter D and the free-stream velocity are unitary ($D = 1$ and $U = 1$).

2.1. Hydrodynamic model

The dynamic of a newtonian, incompressible and isothermal flow can be mathematically represented by partial differential equations of mass and momentum balance, which, respectively, read

$$\nabla \cdot \mathbf{u} = 0, \tag{1}$$

$$\frac{\partial \mathbf{u}}{\partial t} = -\mathbf{u} \cdot \nabla \mathbf{u} - \nabla \Pi + \frac{1}{Re}\nabla^2 \mathbf{u} + \mathbf{f} \tag{2}$$

where, $\mathbf{u}$ and Π are the velocity and pressure field, respectively. The forcing term $\mathbf{f}$ is the surface force imposed by the cylinder, *via IBM*, in order to ensure the no-slip condition on the fluid-solid interface. The non-linear convective term (first on right-side of Eq. (2)) is computed in the skew-symmetric formulation to minimize the aliasing errors.

Eqs. (1), (2) are discretized in a uniform Cartesian grid. Fig. 1 shows a schema of the boundary conditions and some useful geometrical parameters. The initial condition is adopted as an unitary velocity field $\mathbf{u}(x, y, t = 0) = [1\,0\,0]^T$, and the inflow condition is $\mathbf{u}(x = 0, y, t) = [1\,0\,0]^T$. On $y = 0$ and $y = L_y$, the velocity verifies the free-slip condition, while considering a simplified convection equation as outflow ($x = L_x$).

2.1.1. Numerical solution

In order to solve numerically the governing equations (1,2), the `Incompact3D` code is used [26]. The code is based on compact sixth-order finite difference schemes [29] for spatial differentiation and a second-order Adams–Bashforth scheme for time advancement. To treat the incompressibility condition, a fractional step method requires solving a Poisson equation. This equation is fully solved in spectral space via the use of a Fast Fourier Transform.

The cylinders are represented via an *IBM* based on adapted direct forcing method [27]. It allows simple implementation of high-order schemes, for spatial discretization, by adding a forcing term ($\mathbf{f}$) in the fluid momentum equation (Eq. (2)). This term acts only on the grid nodes inside the immersed boundary. The *IBM* is materialized in the time advancement and reflected in the Poisson equation, to solve the pressure field and to ensure the incompressibility condition.

The time advancement method requires to define intermediary velocities (denoted as $\mathbf{u}^*$ and $\mathbf{u}^{**}$). These intermediary velocities are computed by the splitting method:

$$\frac{\mathbf{u}^* - \mathbf{u}^k}{\Delta t} = \frac{3}{2}\mathbf{F}^k - \frac{1}{2}\mathbf{F}^{k-1} - \nabla \Pi^{k-1/2} + \mathbf{f}^{k+1/2}, \tag{3}$$

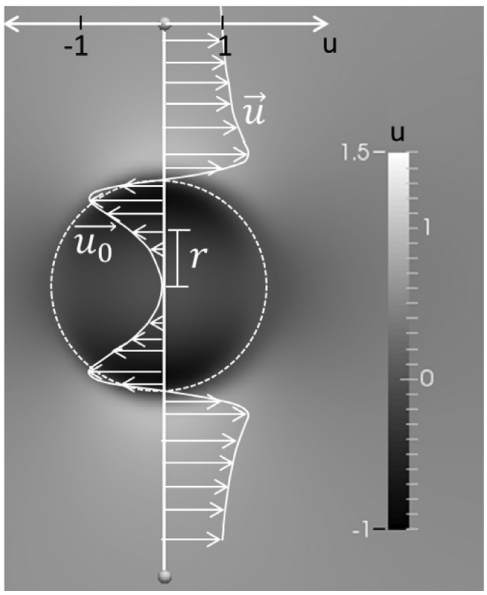

Fig. 2. Immersed boundary method based on mirrored flow. Streamwise velocity inside and outside the cylinder.

$$\frac{\mathbf{u}^{**} - \mathbf{u}^{*}}{\Delta t} = \nabla \Pi^{k-1/2}, \tag{4}$$

$$\frac{\mathbf{u}^{k+1} - \mathbf{u}^{**}}{\Delta t} = -\nabla \Pi^{k+1/2}, \tag{5}$$

here $\mathbf{f}^{k+1/2}$ is estimated by

$$\mathbf{f}^{k+1/2} \approx \mathbf{f}^{*} = \varepsilon \left(-\frac{3}{2}\mathbf{F}^{k} + \frac{1}{2}\mathbf{F}^{k-1} + \nabla \Pi^{k-1/2} + \frac{\mathbf{u}_0^{k+1} - \mathbf{u}^{k}}{\Delta t} \right), \tag{6}$$

where $\mathbf{F}^k$ represents the convective-diffusive term at the instant t^k, Δt is the time step, $\varepsilon(x, y, t)$ is an auxiliary parameter, which is zero outside the cylinder ($\varepsilon = 0$) and one inside ($\varepsilon = 1$). The target velocity field $\mathbf{u}_0^{k+1}$ inside the cylinder is an artificial flow induced by the *IBM*, to ensure smoothness in the velocity (continuity in first derivative) while minimizing spurious oscillations near the fluid-solid interface.

The target velocity at t^{k+1}, in cylindrical coordinates, is computed by

$$\mathbf{u}_0^{k+1}(r, \theta, z, t) \approx \mathbf{u}_0^{*}(r, \theta, z, t) = \mathbf{u}_c^{k+1} + (\mathbf{u}_c^{k+1} - \mathbf{u}^{*}(D - r, \theta, z, t)) \sin\left(\frac{2\pi r^2}{D^2}\right),$$
$$for \qquad 0 \leqslant r \leqslant D/2 \quad and \quad 0 \leqslant \theta < 2\pi, \tag{7}$$

where $\mathbf{u}_c$ is the cylinder velocity and $\mathbf{u}_0$ is a mirrored flow modulated by a, conveniently selected, sinusoidal function in the solid domain (Fig. 2).

The cylinder velocity $\mathbf{u}_c^{k+1}$ is calculated every time step by solving the solid dynamic equation (Section 2.2). The forcing is being applied in $\mathbf{u}_0^{*}$ instead of $\mathbf{u}_0^{k+1}$ (Eq. (7)), inducing a second-order error in time ($error \sim \Delta t^2$). Hence, the second-order accuracy in the time advancement scheme is preserved.

According to Parnaudeau et al. [30], the no-slip condition on the cylinder surface can be assured up to second-order accuracy. Thus, the velocity is reflected by bilinear interpolation.

Applying the divergence operator on both sides of (5), we obtain

$$\nabla^2 \Pi^{k+1/2} = \frac{\nabla \cdot \mathbf{u}^{**} - \nabla \cdot \mathbf{u}^{k+1}}{\Delta t}, \tag{8}$$

where, from incompressibility condition (Eq. (1)), $\nabla \cdot \mathbf{u}^{k+1} = 0$ outside the cylinder but unknown inside, since the internal flow is not physical. Then, to deal with the cylinder(s) movement, some modifications will be proposed on this equation. *For one cylinder*, we consider the following correction to the incompressibility condition

$$\nabla \cdot \mathbf{u}^{k+1} = \nabla \cdot \varepsilon \left(\mathbf{u}_0^{k+1} - \mathbf{u}_c^{k+1} \right) \approx \nabla \cdot \varepsilon \left(\mathbf{u}_0^{**} - \mathbf{u}_c^{k} \right) \tag{9}$$

Substituting (9) in (8), taking $\varepsilon\mathbf{u}_0^{k+1} \approx \varepsilon\mathbf{u}_0^{**}$ and $\mathbf{u}_c^{k+1} \approx \mathbf{u}_c^k$, it follows

$$\nabla^2\Pi^{k+1/2} = \frac{\nabla\cdot\left[(1-\varepsilon)\mathbf{u}^{**} + \varepsilon\mathbf{u}_c^k\right]}{\Delta t}. \tag{10}$$

Analogously, *for two moving cylinders* we have

$$\nabla\cdot\mathbf{u}^{k+1} = \nabla\cdot\left[\varepsilon_1\left(\mathbf{u}_{0_1}^{k+1} - \mathbf{u}_{c_1}^{k+1}\right) + \varepsilon_2\left(\mathbf{u}_{0_2}^{k+1} - \mathbf{u}_{c_2}^{k+1}\right)\right], \tag{11}$$

where the subscripted 1 and 2 represent the cylinder numbering. Then, the Poisson equation for two cylinders can be expressed as

$$\nabla^2\Pi^{k+1/2} = \frac{\nabla\cdot\left[(1-\varepsilon_1-\varepsilon_2)\mathbf{u}^{**} + \varepsilon_1\mathbf{u}_{c_1}^k + \varepsilon_2\mathbf{u}_{c_2}^k\right]}{\Delta t}. \tag{12}$$

Without considering the correction in the incompressibility condition (11), we obtain

$$\nabla^2\Pi^{k+1/2} = \frac{\nabla\cdot\left[(1-\varepsilon_1-\varepsilon_2)\mathbf{u}^{**}\right]}{\Delta t}. \tag{13}$$

For several moving cylinders, the Poisson equation reads

$$\nabla^2\Pi^{k+1/2} = \frac{\nabla\cdot\left[\left(1-\sum_{i=1}^{n_{cyl}}\varepsilon_i\right)\mathbf{u}^{**} + \sum_{i=1}^{n_{cyl}}\left(\varepsilon_i\mathbf{u}_{c_i}^k\right)\right]}{\Delta t}, \tag{14}$$

where $\mathbf{u}_{c_i}$ is the velocity of the i-cylinder, and n_{cyl} is the total number of cylinders. Eq. (14) is completely solved in the spectral Fourier field, then, using Eq. (5), a velocity correction is carried out to compute $\mathbf{u}^{k+1}$. In the right-side of Eq. (13), the divergence is applied to a velocity field which is null inside the cylinder ($\varepsilon_i = 1$) and equal to $\mathbf{u}^{**}$ outside the cylinder ($\varepsilon_i = 0$). As the forcing was already applied on $\mathbf{u}^{**}$, if we are approaching from the fluid to the solid, $\mathbf{u}^{**} \longrightarrow \mathbf{u}_{c_i}^k$, while inside the solid domain, the velocity field is null. It means that, when $\mathbf{u}_{c_i}^k \neq \mathbf{0}$, the Eq. (13) yields a discontinuity at the interface. To overcome this issue, we propose to consider an uniform velocity field equal to the cylinder velocity, inside the solid (Eq. (12), for 2 cylinders or Eq. (14), for n_{cyl} cylinders). By this procedure, the velocity discontinuity is avoided and the internal uniform velocity field is divergence-free. Moreover, it was verified that this consideration stabilizes the code and improves the compact centered schemes performance.

2.2. Dynamic model for cylinders vibration

The elastically-mounted rigid cylinder is modeled as a mass-damping-spring system. The solid motion equation non-dimensionalized by flow parameters (Shiels et al. [31]) is written as

$$m\ddot{x}_j + c\dot{x}_j + kx_j = C_j(t), \tag{15}$$

where x_j, $\dot{x}_j$ and $\ddot{x}_j$ are the cylinder displacement, velocity and acceleration in j-direction ($j = x$ or y). The mechanical parameters (per unit length) are defined as

$$m = \frac{m^*}{\frac{1}{2}\rho D^2} = \frac{\pi}{2}\frac{\rho_c}{\rho}, \quad c = \frac{c^*}{\frac{1}{2}\rho UD} = 2\zeta\sqrt{mk}, \quad k = \frac{k^*}{\frac{1}{2}\rho U^2} = m\left(\frac{2\pi}{U_R}\right)^2 \tag{16}$$

where m is the reduced mass, ρ_c is the cylinder density, c is the mechanical damping coefficient, ζ is the structural damping ratio, k is the structural stiffness coefficient, U_R is the reduced velocity and C_j is the force coefficient in the j-direction. Variables with asterisk represent the corresponding dimensional magnitude. Eq. (15) is numerically solved using a fourth-order Runge–Kutta scheme.

The *FIV* phenomenon is highly dependent on the reduced velocity, which establishes the relation between the solid and fluid time scales. Assuming that the solid time scale (T_{solid}) is estimated through the inverse natural frequency of the system ($1/f_N$) and the fluid time scale (T_{fluid}) by D/U, the following expression is obtained

$$U_R = \frac{T_{solid}}{T_{fluid}} = \frac{U}{f_N D}. \tag{17}$$

2.3. Forces computation

In the present cartesian grid, it is not convenient to compute the force coefficients by integrating the pressure and viscous stresses on the cylinder surface, since an extra interpolation procedure would be required to take the information from the grid nodes to the fluid-solid interface. Conversely, forces are calculated by applying the integral momentum equation in a rectangular control volume (CV) defined around the cylinder (Fig. 3).

The integral momentum equation can be expressed, in the dimensionless form, as

$$\sum\mathbf{F_{ext}} = \mathbf{F_1} + \mathbf{F_2} = \frac{\partial}{\partial t}\int_{VC}\mathbf{u}d\forall + \int_{CS}\mathbf{u}(\mathbf{u}\cdot\mathbf{n})dA, \tag{18}$$

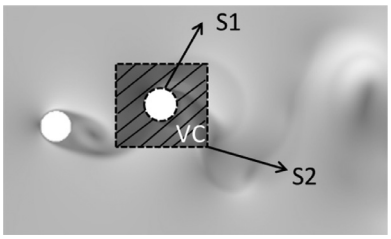

Fig. 3. Control volume to compute the forces on the cylinder surface. The surfaces $S1$ and $S2$ define the volume control boundaries. The background image is an instantaneous field of the velocity magnitude.

Table 1
Convergence analysis of the force coefficients for various spatial uniform resolutions. For domain size $L_x \times L_y = 25 \times 18$, time step $\Delta t = 5 \times 10^{-4}$, cylinders streamwise spacing $S/D = 5$ and Reynolds number $Re = 100$.

$n_x \times n_y$	$\Delta x = \Delta y$	$< C_{D1} >$	$< C_{D2} >$	$C_{L1\,rms}$	$C_{L2\,rms}$	St
501×361	0.050	1.394	0.887	0.319	1.199	0.1617
751×541	$0.03\widehat{3}$	1.385	0.883	0.314	1.191	0.1629
1001×721	0.025	1.384	0.873	0.306	1.162	0.1630

where $\mathbf{F_1}$ and $\mathbf{F_2}$ are the forces per unit cylinder length on the surfaces $S1$ and $S2$, respectively; $\mathbf{n}$ is a unit vector normal to the control surface (CS). From the integration of the pressure and viscous stresses on the surface $S2$, $\mathbf{F_2}$ is computed as

$$\mathbf{F_2} = \int_{S2} \left[-\Pi \ \underline{\mathbf{I}} + \frac{1}{Re}\left(\nabla \mathbf{u} + (\nabla \mathbf{u})^T\right) \right] \mathbf{n} dS. \tag{19}$$

From Eq. (18), and highlighting that there is not flow through $S1$, $\mathbf{F_1}$ is estimated by

$$\mathbf{F_1} = \frac{\partial}{\partial t} \int_{CV} \mathbf{u} d\forall + \int_{S2} \mathbf{u}(\mathbf{u} \cdot \mathbf{n}) dA - \int_{S2} \left[-\Pi \ \underline{\mathbf{I}} + \frac{1}{Re}\left(\nabla \mathbf{u} + (\nabla \mathbf{u})^T\right) \right] \mathbf{n} dS, \tag{20}$$

where, $\underline{\mathbf{I}}$ is the identity matrix. Finally, The force coefficients can be computed using the Cartesian components of $\mathbf{F_1}$:

$$C_D = 2\mathbf{F_1} \cdot \mathbf{e}_x, \tag{21}$$

$$C_L = 2\mathbf{F_1} \cdot \mathbf{e}_y. \tag{22}$$

All simulations in this work were carried out up to $500/\Delta t$ iterations at least. The mean and *rms* of drag (C_D) and lift (C_L) coefficients were computed for the statistically stationary time interval. Then, depending on the simulation, we used around $400/\Delta t$ iterations for the computations.

3. Evaluation of the algorithm

The code `Incompact3D` has been validated and applied to uniform and sheared flow profile past one static cylinder [e.g., [27,32,33]], a single forced oscillating cylinder [34] and a single cylinder subjected to Vortex-induced vibration [33]. A second cylinder, in the wake interference region behind the first cylinder, modifies considerably the flow field and the mechanical response. Hence, in this section, the code is evaluated for two tandem cylinders: (i) fixed with $2 \leqslant (S/D) \leqslant 10$, (ii) in Galilean streamwise translation for $S/D = 3.5$, (iii) with *1dof* cross-stream and initial spacing $(S/D)_0 = (S/D)_c \approx 3.5$.

3.1. Fixed cylinders ($Re = 100$)

To evaluate the code for two fixed cylinders in tandem, simulations for $Re = UD/\nu = 100$ and spacings in the range $2 \leqslant S/D \leqslant 10$ are performed. Results are compared with numerical and experimental studies in terms of mean drag coefficient $< C_D >$, root mean square (*rms*) of the lift coefficient C_{Lrms} and the Strouhal number St ($= f_v D/U$, where f_v is the vortex shedding frequency) behind the rear cylinder. The vortex shedding frequency was calculated from the time series of cross-stream velocity measured by a probe located $5D$ behind the rear cylinder measured along the center-to-center line. In this paper, the subscript 1 is adopted for representing quantities associated to the front cylinder and the subscript 2 for the rear cylinder.

In order to define the mesh resolution, a convergence analysis was performed in a domain size $L_x \times L_y = 25 \times 18$, with three different spatial resolutions, time step $\Delta t = 5 \times 10^{-4}$ and cylinders streamwise spacing $S/D = 5$ (Table 1). The deviation of the forces coefficients between a simulation and its corresponding more refined simulation is around 1%, thereby it was selected the intermediate resolution $n_x \times n_y = 751 \times 541$. The front cylinder position is set to $\left[x_{c_1},\ y_{c_1}\right] = [8,\ L_y/2]$ while

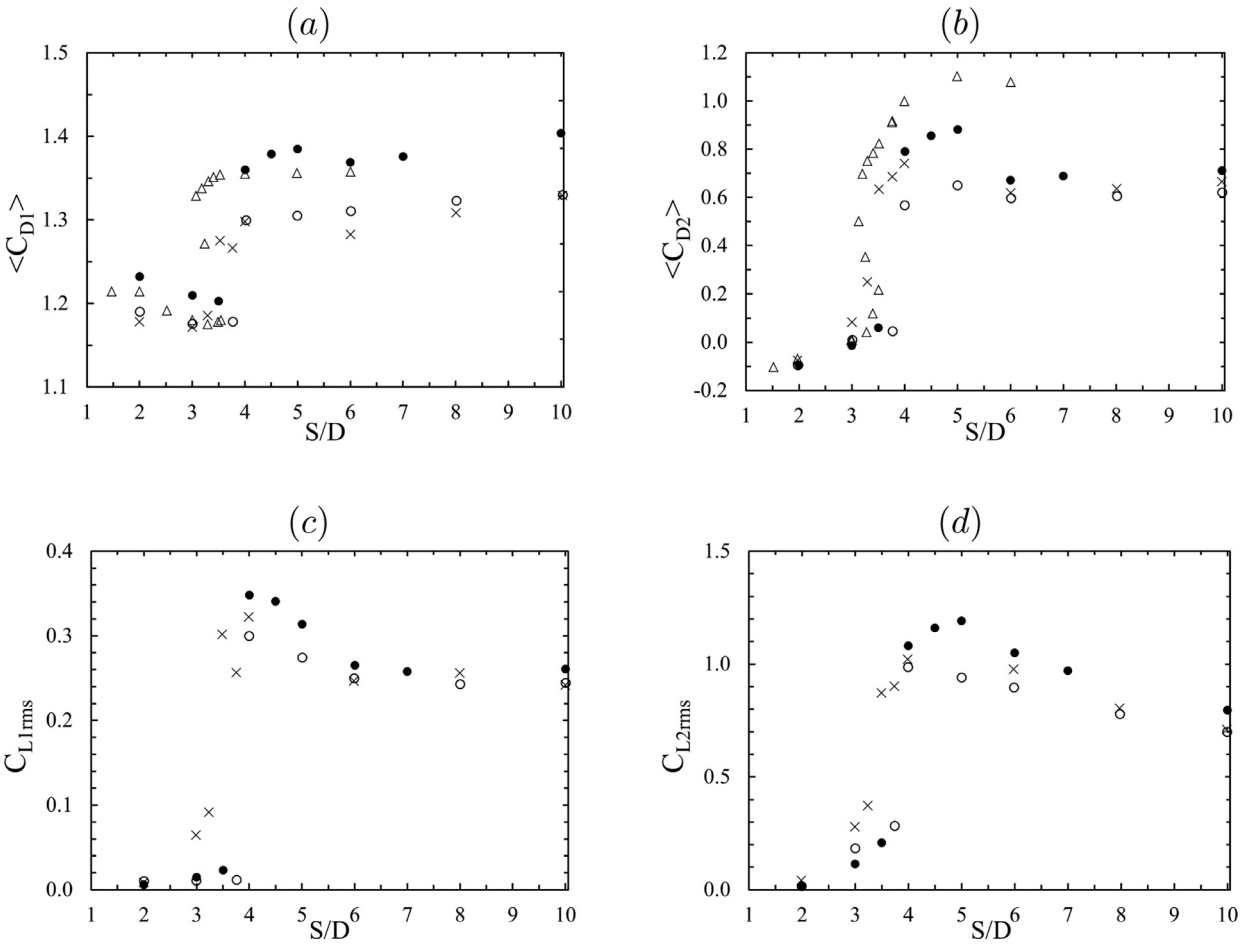

Fig. 4. $< C_D >$ as a function of S/D, for $Re = 100$: (a) front cylinder, (b) rear cylinder. C_{Lrms} as a function of S/D: (c) front cylinder; (d) rear cylinder. • Present study, ○ Sharman et al. [37], × Mussa et al. [39], △ Mizushima and Suehiro [36].

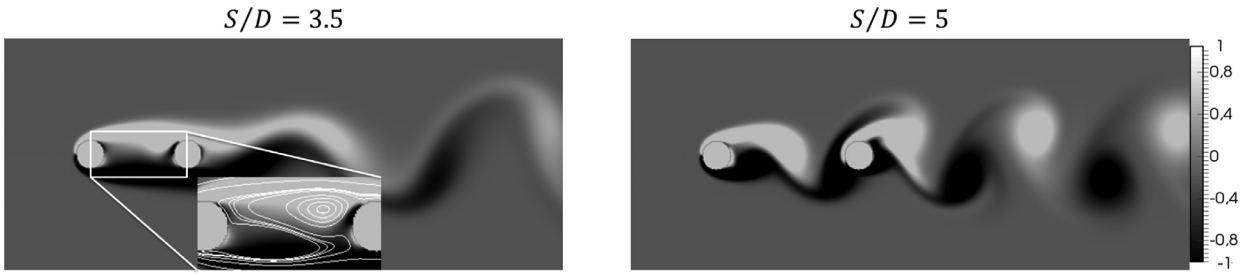

Fig. 5. Vorticity fields. Figure on the left shows the vorticity field and streamlines in the gap before the discontinuity of the force coefficients (unstable reattachment). Figure on the right shows vorticity field after the discontinuity, corresponding to the peak of the lift coefficients fluctuations.

varying the streamwise spacings by moving the rear cylinder position in downstream direction. For $S/D = 10$, the domain size in the streamwise direction is increased to $L_x = 35$ to avoid interference at the outlet.

Force coefficients are in good agreement with numerical works (Fig. 4). The greatest difference of $< C_{D1} >$ (Fig. 4a) relative to other numerical studies is close to 4%. For $S/D = (S/D)_c \approx 3.5$, the signal inversion of $< C_{D2} >$ is adequately reproduced and the vorticity field shows appropriate representation of the unstable reattachment (Fig. 5). It is particularly interesting the upper-branch identified for $< C_{D2} >$, C_{L1rms} and C_{L2rms} (Fig. 4b, c and d, respectively) in the range $4 \leqslant S/D \leqslant 5$. Such upper-branch is associated with the cylinders proximity after the force coefficients discontinuity, for which the wake is completely developed in the gap (left-side of Fig. 5).

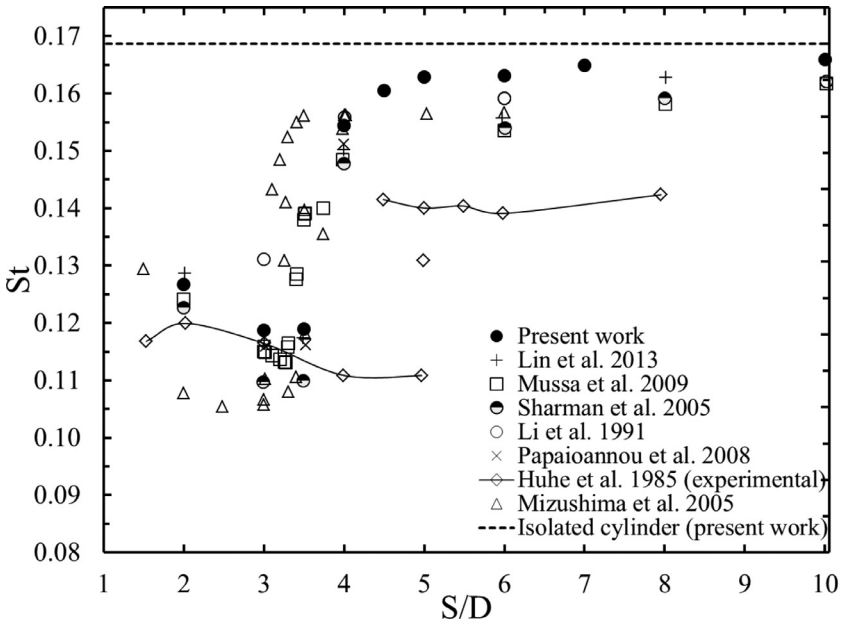

Fig. 6. Strouhal number *St* behind the rear cylinder, as a function of center-to-center spacing *S*/*D*.

The Strouhal number *St* has a good agreement with the reference numerical studies (Fig. 6). For $S/D > 3.5$ and $Re = 100$, the experimental study [13] shows surprisingly low values of *St* if it is compared to the numerical results [23,35–39]. However, the experimental results for $Re = 300$ fit better with the numerical studies, at this interval.

3.2. Evaluation of formulation for Galilean translation (Re = 40)

In order to verify the beneficial effects of the algorithm for representing moving multiple bodies, 2*D* simulations for $Re = 40$ are performed. Galilean invariance is considered, which means that there must not be differences between two fixed cylinders and the equivalent moving cylinders (streamwise movement) relative to the Eulerian mesh. This invariance is evaluated in terms of the streamwise velocity profile (u_x) through the cylinder center ($x = x_{c_i},\ i = 1, 2$) and along the middle of gap.

For fixed cylinders, the computational domain ($L_x \times L_y = 20 \times 12$) and resolution ($n_x = 361,\ n_y = 217$) are selected as defined by Parnaudeau et al. [27]. The cross-stream position of the front cylinder is $y_{c_1} = L_y/2 = 6$ and the streamwise position is $x_{c_1} = 8$. For moving cylinders, the computational domain is $L_x \times L_y = 40 \times 12$ and the number of nodes in x is incremented to $n_x = 721$, to maintain the spatial resolution.

Finally, for fixed cylinders the free stream velocity is **U**, while, for moving cylinders, it is **U**/2 and the cylinders velocity is set to $-\mathbf{U}/2$. Thus, the Reynolds number remains the same for both cases. The center-to-center spacing and the time step were set to $S/D = 3.5$ and $\Delta t = 1 \times 10^{-3}$, respectively.

The results obtained using the new proposed Poisson equation (12), with the incompressibility condition corrected, fit better to the fixed cylinders results than the results obtained without correction (Eq. (13)), as Fig. 7 shows. The differences between the two approaches can be observed especially in the boundary layers and in between the two cylinders.

3.3. Cylinders submitted to FIV

In this section, the algorithm is evaluated for a single cylinder and two cylinders in tandem elastically mounted with one degree of freedom (*1dof*) to oscillate in cross-stream direction. Table 2 shows the structural and flow parameters associated with the configurations simulated. Table 3 displays the domain size and the parameters for the spatial and temporal discretization. The formulation is evaluated in terms of the maximum cross-stream oscilation amplitudes $(y/D)_{max}$ as a function of the reduced velocity $U_R = U/(f_N D)$. It is important to stress that the low reduced velocity U_R is associated with high natural vibration frequency f_N (quick solid response), while high values of U_R implies low values of f_N (slow solid response).

Fig. 8 presents the maximum cross-stream oscillation amplitude $(y/D)_{max}$ against the reduced velocity U_R, for the verification scenarios. This figure shows the results obtained in this paper compared with the results presented in Griffith et al. [17] and in Borazjani and Sotiropoulos [16]. The largest deviations relative to the reference studies occur for $4 \leqslant U_R \leqslant 5$, where the rear cylinder response curve seems to be shifted around 0.5 reduced velocity units. But nevertheless, the resonance range and the behavior of the response curves are similar.

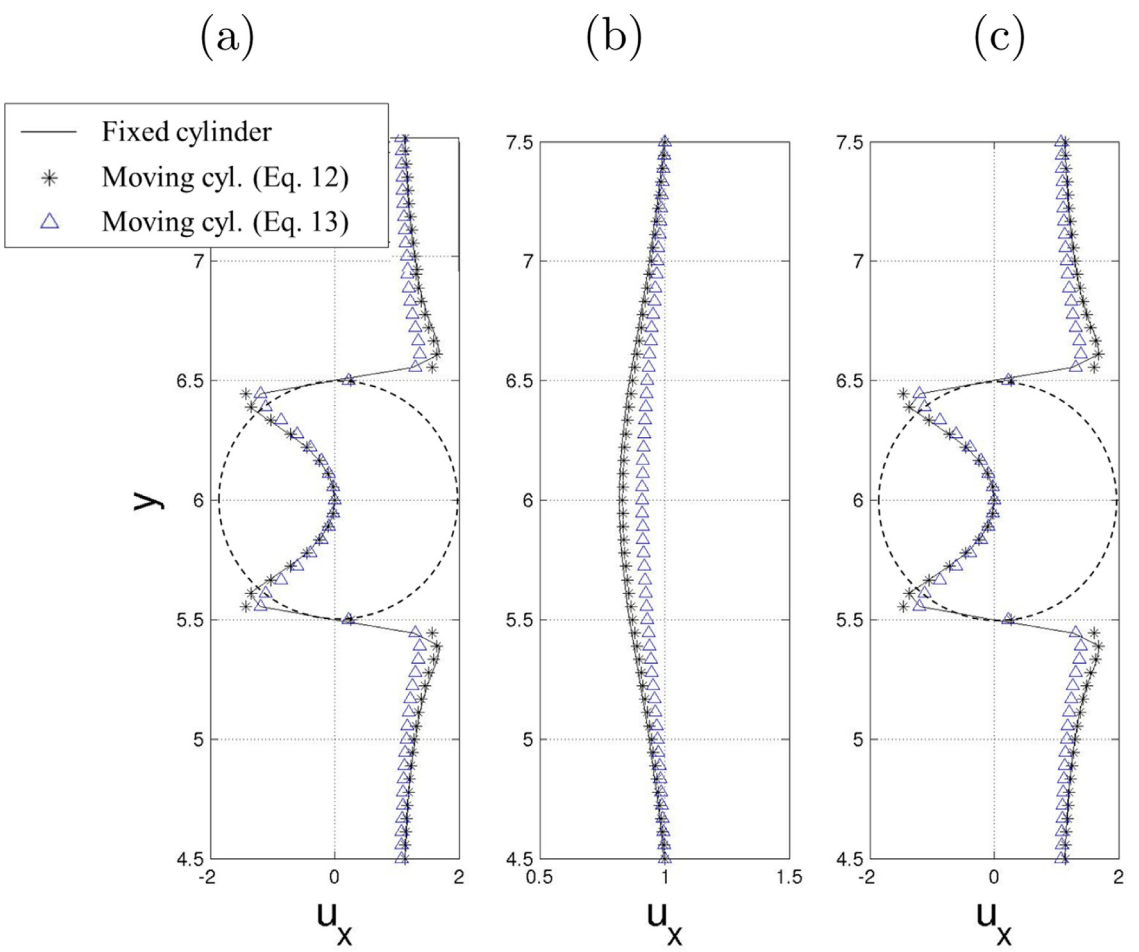

Fig. 7. Streamwise velocity profiles for $Re = 40$. Comparison between fixed (continuous line) and moving cylinders with ($*$) and without the new Poisson equation ($\triangle$). (a) Profile through the front cylinder; (b) profile in the middle of the gap between cylinders; (c) profile through the rear cylinder.

Table 2
Structural and flow parameters of simulations for cylinders in induced vibration (*VIV* and *FIV*). $(S/D)_0$ is the initial streamwise center-to-center spacing.

	Degrees of freedom	*Re*	$(S/D)_0$	*m*	ζ	U_R
Verification scenarios						
I	1 *dof* (single cylinder)	200	–	4	0	(3 – 9)
II	1 *dof* (two cyl. in tandem)	200	1.5	4	0	(3 – 9)
Application scenarios (two cylinders in tandem)						
III	1 *dof*	200	3.5	1	0.007	(2 – 14)
IV	2 *dof*	200	3.5	1	0.007	(2 – 14)
V	1 *dof*	300	3.5	1	0.007	(2 – 14)
VI	2 *dof*	300	3.5	1	0.007	(2 – 14)

Table 3
Parameters for the spatial and temporal discretization.

	n_x	n_y	L_x	L_y	Δt
Verification scenarios					
I	721	649	20	18	5×10^{-4}
II	751	541	25	18	5×10^{-4}
Application scenarios					
III	901	721	25	20	5×10^{-4}
IV	901	721	25	20	5×10^{-4}
V	1001	801	25	20	5×10^{-4}
VI	1001	801	25	20	5×10^{-4}

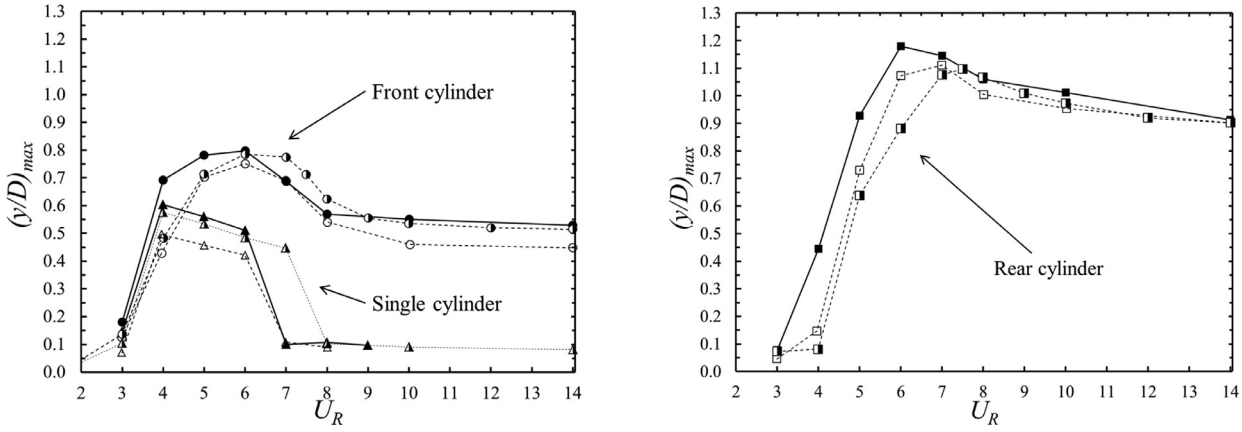

Fig. 8. Maximum cross-stream displacement $(y/D)_{max}$ as a function of reduced velocity (U_R), for $Re = 200$, $S/D = 1.5$, $m = 4$ and $\zeta = 0$. Single cylinder: (▲) present study, (△) Borazjani and Sotiropoulos [16], (◮) Griffith et al. [17]; front cylinder: (●) Present work, (○) Borazjani and Sotiropoulos [16], (◑) Griffith et al. [17]; rear cylinder: (■) present study, (□) Borazjani and Sotiropoulos [16] and (◨) Griffith et al. [17].

4. Flow-induced vibration

Considering the results obtained, the formulation can be applied for two elastically mounted cylinders in tandem with *1dof* and extended to cylinders with *2dof*. In this section, results of application scenarios (corresponding to simulations from III to VI in Tables 2 and 3) are analyzed. The initial streamwise spacing $(S/D)_0$ is set to 3.5, which is close to the critical one $(S/D)_c$ for fixed cylinders, although $(S/D)_c$ slightly decreases as the Reynolds number increases. For this initial spacing, the rear cylinder is located at the start of the wake interference region where the wake energy is the highest (as reflected in C_{L2rms}, interpreting the *rms* like an energy measurement, Fig. 4b). This, in addition to a low mass-damping parameter ($m\zeta$), aims to achieve high oscillation amplitudes and large synchronization range.

4.1. $Re = 200$

The results discussed in this subsection are based on the parameters defined by the simulations III and IV (Tables 2 and 3) corresponding to *1dof* and *2dof* scenarios, respectively. As for a single cylinder, the response of a tandem arrangement shows a strong dependence on the reduced velocity (Borazjani and Sotiropoulos [16]). Hence, almost all the variables are analyzed as a function of this parameter.

Fig. 9 displays the cross-stream oscillation amplitude A_y, the relation between oscillation frequency to natural frequency f/f_N and the Strouhal number St as a function of the reduced velocity U_R, for the scenarios with *1dof* and *2dof*.

For *1dof* (left column of Fig. 9), the cross-stream oscillation amplitude A_y of the front cylinder is practically the same as for a single cylinder (Fig. 9a), but the lock-in region is shorter ($5 \leqslant U_R \leqslant 8$ in Fig. 9b). Out of lock-in region, the Strouhal number St of *1dof* single cylinder is different from that for two cylinders in tandem (Fig. 9c). As predicted by lock-in definition $f \approx f_N$ (Fig. 9*b*), the St decreases in this region, approximately, according to the relation $St = 1/U_R$. Out of lock-in, the Strouhal number St trends to stabilize in lower values than those of a fixed single cylinder ($St \approx 0.20$).

For *2dof* scenario (right column of Fig. 9), the front cylinder has higher amplitudes A_y (Fig. 9d) and shorter lock-in range (Fig. 9e) than a single cylinder. Rear cylinder does not show clearly a lock-in interval (Fig. 9e), but it reveals $f/f_N < 1$ (or $f < f_N$). Fig. 9e displays the frequency ratio f/f_N relative to the most energetic oscillation frequency f, although in the oscillation spectrum there were identified slightly lower energetic harmonics of f (not shown here), which fit better with the lock-in condition $f/f_N \approx 1$. As observed for *1dof*, for *2dof*, the Strouhal number St trends to stabilize in lower values than those of fixed single cylinder (Fig. 9f).

The cross-stream oscillation amplitude A_y is higher for the rear cylinder than for the front cylinder, except within the interval $3.75 < U_R < 4.5$ (Fig. 9a), for *1dof* scenario, and within $3.75 < U_R < 5$ (Fig. 9d), for *2dof* scenario. This effect starts around the reduced velocity region in which the Strouhal number St has a peak (Fig. 9c and f) and finishes when the lock-in starts (Fig. 9b and e). In order to understand this effect, the pressure field, vorticity field, lift force, cylinders displacement and velocity are analyzed for one oscillation cycle and *1dof* scenario (Fig. 10). The pressure field around the front cylinder shows high- (stagnation region) and low-pressure pockets, while around the rear cylinder, lower pressure magnitudes are developed. However, the lift force acting on both cylinders has the same order of magnitude. At instants A and C, (conversely to the result reported by Borazjani and Sotiropoulos [16], for $S/D = 1.5$) a significant stagnation region arises on the rear cylinder surface, resulting in a high lift force acting in opposite direction to the movement. This is because the external flow partially enters the gap region, confining or controlling the rear cylinder movement (low cylinder velocities and oscillation amplitudes) through the development of this stagnation region. Here, this effect will be referred to as *confinement effect*.

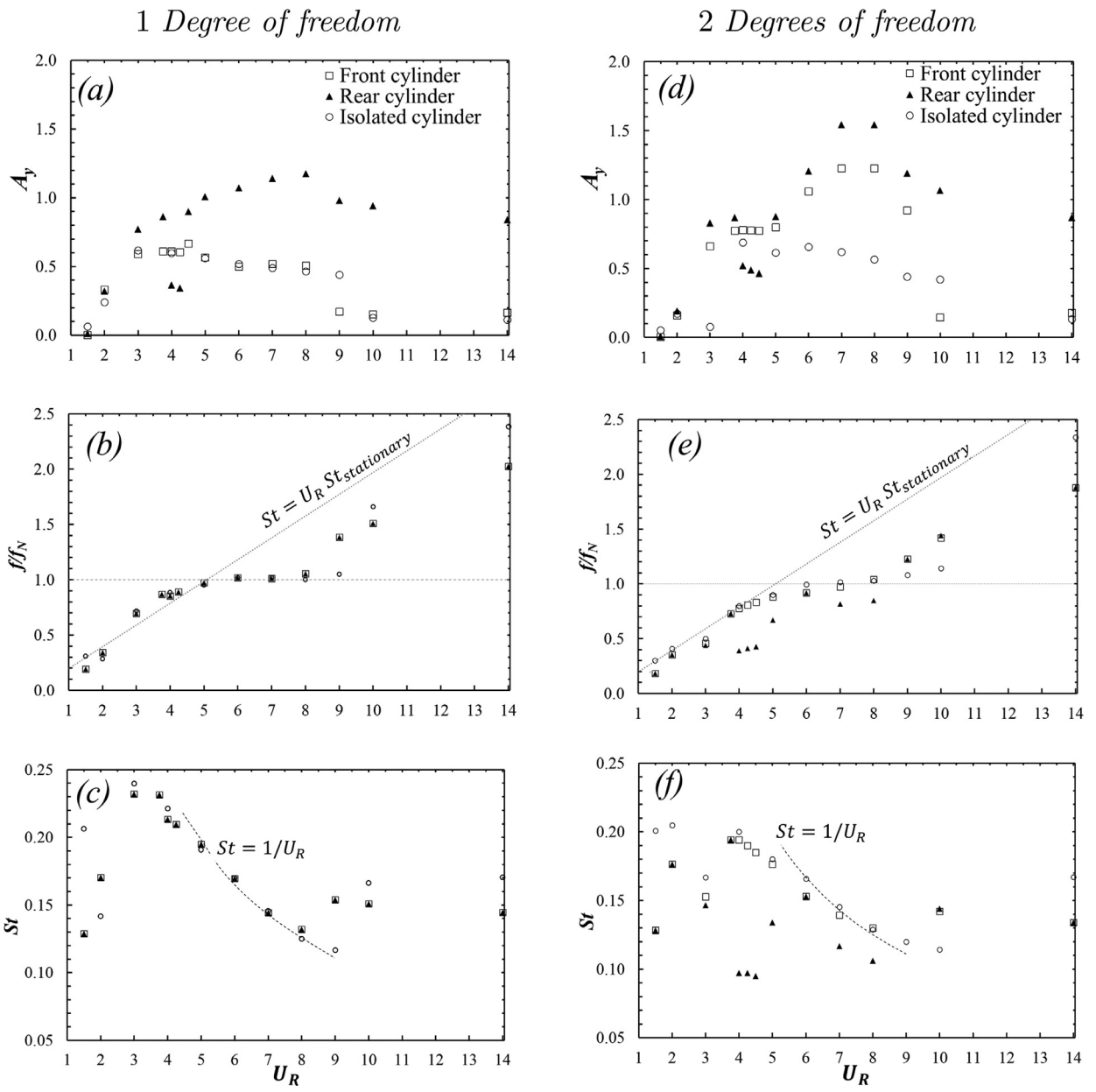

Fig. 9. Flow-induced vibration of two cylinders in tandem ($Re = 200$, $S/D = 3.5$, $m^* = 1$, $\zeta = 0.007$). Left: *1dof*, right: *2dof*. (*a, d*) A_y: Cross-stream oscillation amplitude ; (*b, e*) f/f_N: oscillation frequency to natural frequency; (*c, f*) St : Strouhal number.

Analyzing the signals of lift force, displacement and velocity, it can be observed that, C_{L_1} is approximately in-phase with y_1/D and C_{L_2} is approximately in anti-phase with V_{cyl_2}. This roughly suggests that the flow acts as a negative spring on the front cylinder ($C_{L_1} \propto +y_1/D$, maintaining high oscillations) and as a damper on the rear cylinder ($C_{L_2} \propto -V_{cyl_2}$, maintaining low oscillations). In contrast, it is interesting to note that, for $S/D = 1.5$, $U_R = 4$ and *no structural damping* (Borazjani and Sotiropoulos [16]), the lift force is in-phase with the cylinder displacement ($C_{L_2} \propto +y_2/D$). The same effect is reported by Assi et al. [2], who performed physical and numerical experiments at different Reynolds numbers and streamwise spacing $S/D = 4$, for fixed front cylinder and 1*dof* rear cylinder. For no mechanical spring ($k = 0$ or $U_R = \infty$ in Eq. (15)), they found that the wake acts as a spring on the rear cylinder (It was so-called "wake stiffness"). This is also reported by Carmo et al. [20], for the same degrees of freedom, but considering $S/D = 3$, $Re = 150$ and $k \neq 0$.

On the other hand, in the vorticity fields can be identified that the rear cylinder is always inside the upstream wake. Moreover, the downstream combined wake is not a regular Von Karman street since vortexes shed from the front cylinder disrupts and consequently modifies the vortex detachment from the rear cylinder.

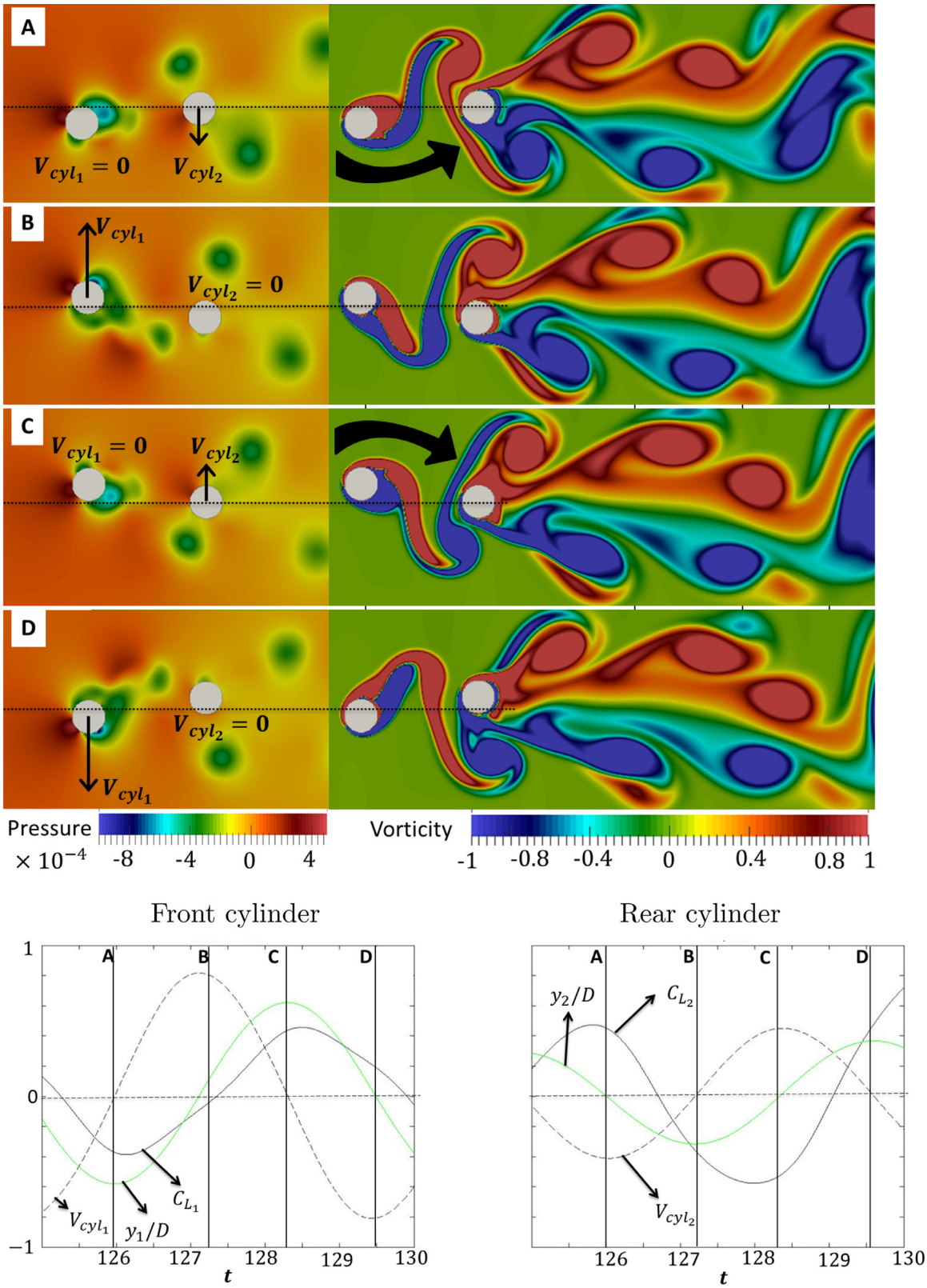

Fig. 10. Instantaneous pressure fields (up left) and vorticity (up right) for two tandem cylinders submitted to *FIV* (*1dof*, $Re = 200$, $S/D = 3.5$, $m^* = 1$, $\zeta = 0.007$ and $U_R = 4$). Bottom: time series of lift coefficient (C_L), cylinder cross-stream velocity (V_{cyl}) and cylinder cross-stream displacement (y/D) relative to the initial position. The black arrows in the pressure fields represent the cylinder velocity vector. The curved black arrows in the vorticity fields illustrate the confinement effect of the external flow over the free shear layers around the rear cylinder.

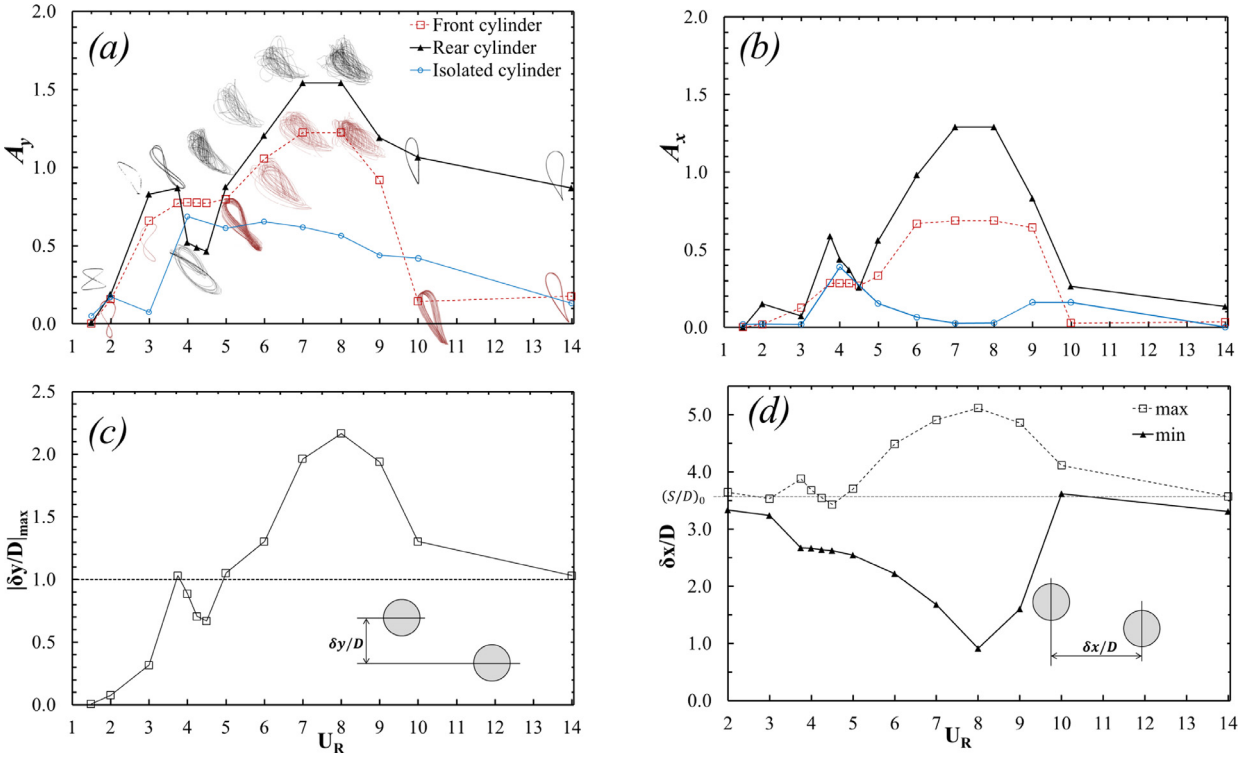

Fig. 11. Oscillation amplitudes (a, b) and extreme center-to-center spacings (c, d) as a function of reduced velocity, for scenario with *2dof*, $Re = 200$, $(S/D)_0 = 3.5$, $m^* = 1$ and $\zeta = 0.007$. (*a*) A_y: Cross-stream oscillation amplitude; (*b*) A_x: streamwise oscillation amplitude; (*c*) $|\delta y/D|_{max}$: maximum cross-stream spacing; (*d*) $(\delta x/D)_{max}$, $(\delta x/D)_{min}$: maximum and minimum streamwise spacing.

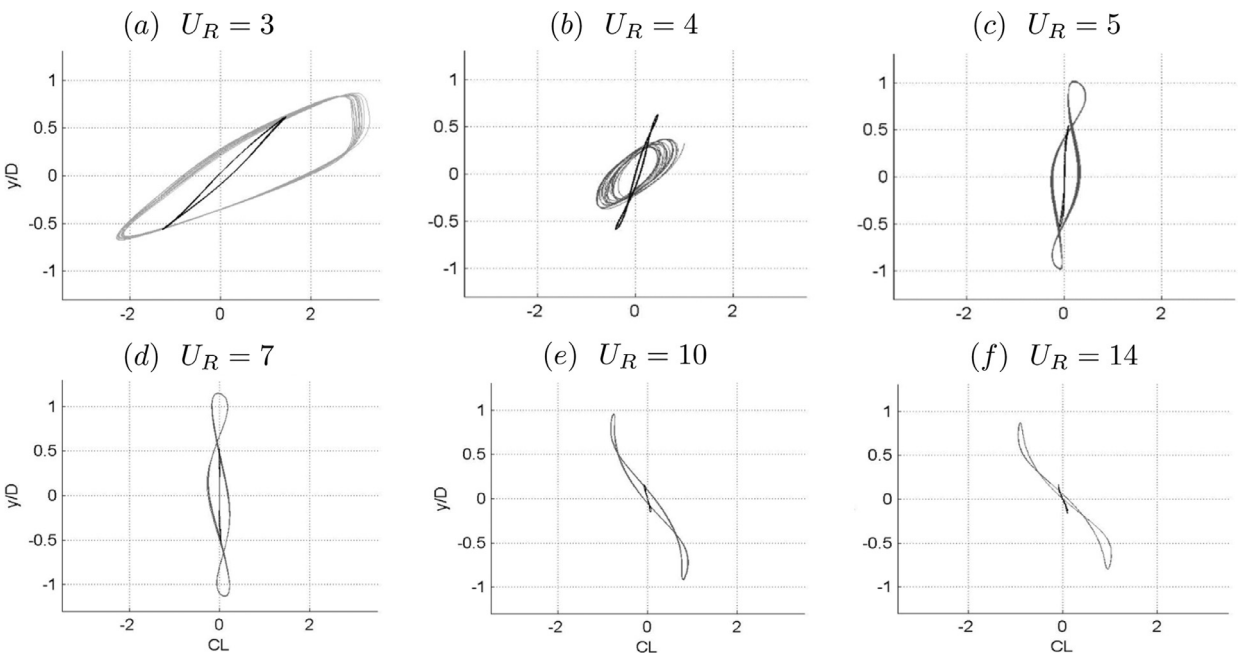

Fig. 12. Phase portrait of the lift coefficient relative to the transverse motion for the 1*dof* tandem system ($Re = 200$, $S/D = 3.5$, $m^* = 1$, $\zeta = 0.007$). Black and grey colors correspond to the front and the rear cylinders respectively.

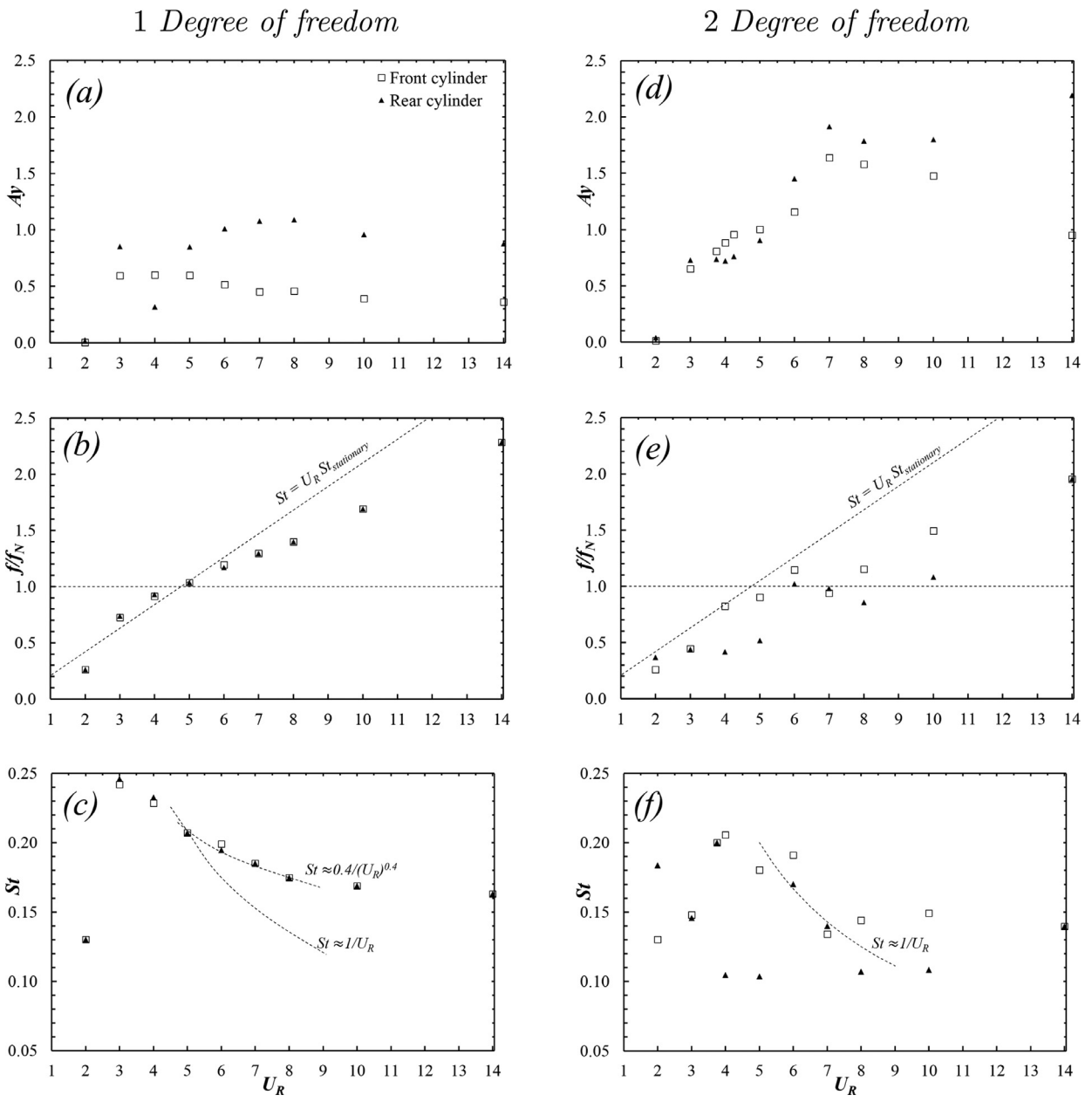

Fig. 13. Flow-induced vibration of two cylinders in tandem ($Re = 300$, $(S/D)_0 = 3.5$, $m^* = 1$, $\zeta = 0.007$). (*a, d*) Response curve: cross-stream oscillation amplitude A_y; (*b, e*) f/f_N: oscillation frequency to natural frequency; (*c, f*) St : Strouhal number.

Fig. 11 a displays the cross-stream oscillation amplitude A_y and the cylinders trajectories as a function of the reduced velocity U_R. Front cylinder trajectories have eight-shape for $U_R < 5$, drop-shape for $U_R > 8$, and an irregular transition between these shapes for lock-in interval ($5 \leqslant U_R \leqslant 8$). From the inclination of some trajectories, it can be inferred that the maximum cross-stream oscillation, approximately, coincides with minimum stream-wise one (left-top branch of the trajectory loop), and, inversely, when y/D is minimum, x/D is maximum (right-bottom branch of the trajectory loop). This means that the time histories of the cross-stream y/D and stream-wise x/D oscillations are approximately in anti-phase.

In the lock-in region, a single cylinder does not show considerable streamwise amplitude oscillations A_x (Fig. 11b) and concentrates the energy, transferred from the fluid, in cross-stream amplitude oscillations (A_y). On the other hand, in *2dof* cylinders, the distribution of energy between cross-stream and streamwise oscillations could lead to *dual resonance* [40]. It means that, the lock-in region of the cross-stream oscillations could coincide with those of the streamwise oscillations. Thus, A_x could not to be negligible in relation to A_y (Fig. 11a and b). Nevertheless, for high reduce velocities ($U_R > 9$, where the galloping normally occurs) $A_y > A_x$.

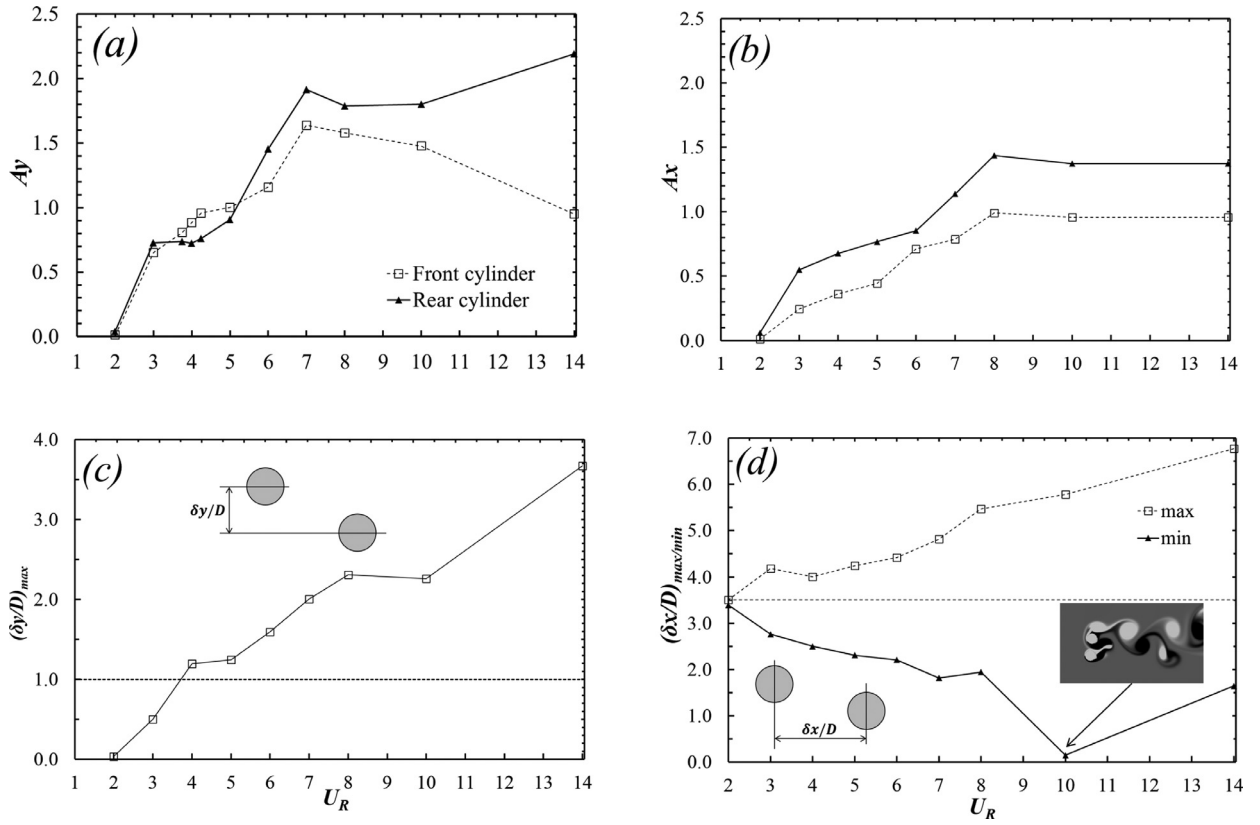

Fig. 14. Oscillation amplitude and extreme relative spacing as a function of reduced velocity. (*a*) Cross-stream oscillation amplitude A_y; (*b*) Streamwise oscillation amplitude A_x; (*c*) Maximum cross-stream spacing $(\delta y/D)_{max}$; (*b*) Maximum and minimum Streamwise spacing. Scenario with *2 dof*, for $Re = 300$, $(S/D)_0 = 3.5$, $m^* = 1$ and $\zeta = 0.007$.

For *2dof*, in the confinement effect interval, from $U_R = 3.75$ to $U_R = 4.5$, the rear cylinder oscillations and the Strouhal number (A_y, A_x and St) decrease around 50% (▲ in Fig. 11a, b and f). Furthermore, in this interval, the maximum center-to-center cross-stream spacing is $|\delta y/D|_{max} < 1$, while $|\delta y/D|_{max} > 1$ for $U_R > 4.5$ (Fig. 11c). When $|\delta y/D|_{max} > 1$, a vertical gap allows activating the gap-flow-switch mechanism [41], stimulating the galloping instability. On the other hand, the peak center-to-center streamwise spacing ($\delta x/D$), is greater in the lock-in and practically negligible out of lock-in (Fig. 11d). Using a mechanical admittance function, an excitation (e.g. C_L, C_D) can be transformed in a response (e.g. y/D, x/D). This assumption is satisfactory when the response does not modify considerably the excitation, but in fluid-structure interaction framework, the excitation and response coexist and have a non-linear relation. This complex interaction can be represented in an Excitation-Response plane, as Fig. 12 ($y/D - C_L$) shows, for *1dof* scenario. From this figure, aspects related to the phase and frequency relations, between C_L and y/D, can be inferred. In the *VIV* literature, these plots are also referred to as phase portraits or Lissajous curves. At the points where $\partial(y/D)/\partial C_L = \infty$, C_L has extreme values, which are maximum in the first and fourth quadrants and minimum in the second and third quadrants. Analogously, where $\partial(y/D)/\partial C_L = 0$, y/D has a maximum in the first and second quadrants and a minimum in the third and fourth quadrants. Curves with positive inclination represent cases close to in-phase condition, since both maximum (or minimum) C_L and y/D values coincide in the same quadrant. Conversely, negative inclinations are associated to anti-phase conditions. Therefore, for $U_R \leqslant 4$, the variables are in-phase; in the lock-in ($5 \leqslant U_R \leqslant 8$ in Fig. 9b), low values of C_L yield large variations of y/D; for $U_R \geqslant 10$, the variables are in anti-phase. During a closed cycle along the curve, the number of maximum (or minimum) of C_L and y/D can be counted and the relation between frequencies will be directly linked to these number of extreme values. For instance, in the lock-in (Fig. 12c and d), C_L has three maximum values in a cycle, while y/D has one. Thus, the fluctuation frequency of C_L is three times higher than the frequency of y/D. In Fig. 12, the higher frequencies were filtered, in order to consider only the more energetic frequencies in the analysis.

4.2. $Re = 300$

It is well known that, for a fixed cylinder, tree-dimensional flow structures are developed at flow about $Re = 180 - 194$ [42]. Thus, as the 3D flow structures are not developed in 2D simulations, the energy which should be dissipated by these flow structures, now, is concentrated in the 2D flow structures. This energy could eventually be transfered to the cylinders,

amplifying artificially the oscillations. However, it has been shown that cylinder oscillations tend to suppress the 3D flow, remaining 2D flow behavior up to $Re = 280$, as it was found by Leontini et al. [43], for a transversely oscillating cylinder. Anyway, we consider that this scenario with $Re = 300$, is an interesting condition to test our algorithm and evaluate the implications of the non-dissipated energy. As we are aware of this, in this section the 1*dof* simulations show that, in the lock-in, this energy could be concentrated in higher frequencies than the corresponding to the resonance condition $f = f_N$.

For 1*dof*, the confinement effect is identified for $U_R = 4$ (Fig. 13a) and the lock-in was practically eliminated (Fig. 13b). This phenomenon so-called *soft lock-in* [44] has also been reported in other papers [e.g., [45–47]]. Mittal and Kumar define *soft lock-in* as one of the mechanisms in nonlinear oscillators to self-limit the vibration amplitude. As a *soft lock-in* consequence, the *St* (Fig. 13c) does not decreases with the relation $St \approx 1/U_R$, but with the relation $St \approx 0.4/(U_R)^{0.4}$ in the range $5 \leqslant U_R \leqslant 8$. For $U_R > 8$, *St* tends to stabilize in lower values (≈ 0.16) than the associated to fixed single cylinder ($St \approx 0.21$).

For *2dof* scenario, the confinement effect is identified in the range $3 < U_R < 6$ (Fig. 13d) and the lock-in is more evident for front cylinder in the range $4 \leqslant U_R \leqslant 5$ (Fig. 13e). The galloping instability induces the highest oscillation of the rear cylinder, for $U_R = 14$. Despite of the cross-stream oscillation amplitudes are higher than those corresponding to $Re = 200$, for *2dof* scenario, the behavior of the frequency ratio f/f_N (Fig. 13e) and of the Strouhal number *St* (Fig. 9f) is similar.

The *dual resonance* and *galloping* development make the streamwise oscillation amplitudes not negligible related to the cross-stream oscillation amplitudes (Fig. 14a and b). The cross-stream and streamwise (Fig. 14c and d) extreme center-to-center spacing increase as the reduced velocity increases. For $U_R = 10$, $(\delta x/D)_{min}$ is closed to zero, which could mean crashing or, at least, increasing of crashing risk (Fig. 14d). However, in the simulations, the cylinders did not crash.

5. Conclusions

In this paper, we study numerically the flow-induced vibration of two circular cylinders in tandem arrangement at low Reynolds numbers *Re* and center-to-center streamwise spacing S/D around the critical one $(S/D)_c$. Three scenarios are analyzed: (i) fixed cylinders and various spacings at $Re = 100$, (ii) Galilean streamwise translations at $Re = 40$, (iii) elastically mounted cylinders with one and two degrees of freedom at $Re = 200$ and 300. For scenario (iii) the mass ratio m and the damping ζ are set to 1 and 0.007. For scenario (i), we analyze the drag coefficient C_D, the lift coefficient C_L and the Strouhal number *St* as a function of the streamwise spacing. In scenario (ii), we evaluate the algorithm in terms of the streamwise velocity profiles. Finally, for scenario (iii), we investigate the cross-stream A_y and streamwise A_x cylinders oscillations, the frequency ratio f/f_N, the Strouhal number. The relative distance between cylinders, the lift coefficient and the cylinder displacement in function of the reduced velocity U_R.

To achieve the foregoing goals, the high-order precision code `Incompact3D` is applied as fluid dynamics solver. It is required to develop and evaluated a formulation, for the Poisson equation to solve the pressure field, which allows coupling the fluid and multiple solid movement by using an immersed boundary method. The code `Incompact3D`, with the proposed Poisson equation, represented satisfactorily the Galilean invariance between two fixed cylinders in tandem and the equivalent moving cylinders case. It is also capable of representing phenomena arising from the fluid/solid interaction, as the galloping instability (also referred to as wake-flutter) and resonance.

In the range of adopted parameters in simulations, the scenarios with two degrees of freedom (*2dof*) always are more critical than those with one degree of freedom (*1dof*) in terms of oscillation amplitudes. It should be pointed out that, for *2dof*, the streamwise oscillations amplitudes are not negligible relative to the cross-stream oscillation amplitudes. It means that the streamwise degree of freedom allows the rear cylinders to be placed in different wake interference points and, eventually, closer to the front cylinder. Hence, the cylinders clashing risk increases, especially when the wake-flutter mechanism is activated.

For $3.5 < U_R < 5.0$, a confinement effect was identified in which the cross-stream oscillation amplitude A_y of rear cylinder is lower than that of front cylinder. This is due to the upstream wake acts as a mechanical damper on the rear cylinder. This was not reflected on Strouhal number *St* or the frequency ratio f/f_N, for *1dof*. For *2dof* the effect is reflected in energy transfer from A_y to A_x, which can also be identified in the subharmonics of the $St-U_R$ and $f/f_N - U_R$ graphs. On the other hand, for *2dof*, when the Reynolds number increases the crashing risk also increases, since the cylinders proximity is narrowed.

For $Re = 200$, the trajectories are well defined out from the lock-in region. Typically, trajectories are eight-shaped (two loops) for $5 < U_R$, and drop-shaped for $U_R > 8$. The first case indicates that streamwise oscillation frequency is twice the cross-stream ones, while the second one shape indicates the same frequencies in both direction oscillations.

Acknowledgments

This work was supported by the National Council of Technological and Scientific Development (Conselho Nacional de Desenvolvimento Científico e Tecnológico, *CNPq*), Brazil. This study was granted access to the HPC resources of the “Núcleo avançado de computação de alto desempenho” (NACAD/COPPE - UFRJ), under the platform LoboC.

References

[1] C.H.K. Williamson, R. Govardhan, Vortex induced vibrations, Annu. Rev. Fluid Mech. 36 (2004) 413–455.
[2] G.R.S. Assi, B.S. Carmo, P.W. Bearman, S.J. Sherwin, J.R. Meneghini, The concept of wake stiffness in the wake-induced vibration of a tandem cicular cylinders, in: Proceedings of IUTAM Symposium on Bluff Body Wakes and Vortex-Induced Vibration, Campri Island, 2010, pp. 55–58.

[3] T. Igarashi, Characteristics of the flow around two circular cylinders arranged in tandem (1st report), Bull. Jpn. Soc. Mech. Eng. 24 (1981) 323–331.
[4] D. Sumner, S.J. Price, M.P. Païdoussis, Flow-pattern identification for two-staggered circular cylinders in cross-flow, J. Fluid Mech. 411 (2000) 263–303.
[5] M.M. Zdravkovich, Flow Around Circular Cylinders. A Comprehensive Guide Trough Flow Phenomena, Experiments, Appications, Mathematical Models, and Computer Simulations, Oxford University Press, 2003.
[6] M.P. Païdoussis, S.J. Price, E. Langre, Fluid-Structure Interaction, Cross-Flow Induced Intabilities, 2nd ed., Cambridge University Press, New York, USA, 2014.
[7] M.P. Païdoussis, Real-life experiences with flow-induced vibration, J. Fluids Struct. 22 (2006) 741–755.
[8] D. Sumner, Two circular cylinder in cross-flow: a review, J. Fluids Struct. 26 (2010) 849–899.
[9] G.F. Narváez, Análise Numérica da Vibraço Induzida por vórtices de Dois Cilindros em Alinhados Com o Escoamento, Universidade Federal do Rio Grande do Sul. Instituto de Pesquisas Hidráulicas. Programa de Pós-Graduação em Recursos Hídricos e Saneamento Ambiental, Porto Alegre, 2015 Master's thesis.
[10] M.M. Zdravkovich, Flow induced oscillations of two interfering circular cylinders, J. Wind Eng. Ind. Aerodyn. 101 (1985) 511–521.
[11] D. Brika, A. Laneville, The flow interacion between a stationary cylinder and a downstream flexible cylinder, J. Fluids Struct. 13 (1999) 579–606.
[12] M.M. Alam, M. Moriya, K. Takai, H. Sakamoto, Fluctuating fluid force acting on two circular cylinders in a tandem arrangement at a subcritical Reynolds number, J. Wind Eng. Ind. Aerodyn. 91 (2003) 139–154.
[13] A. Huhe, M. Tatsuno, S. Taneda, Visual studies of wake structure behind two cylinders in tandem arrangement, in: Reports of Research Institute for Applied Mechanics, Kyushy University, 1985, p. 99.
[14] M. Kiya, M. Arie, H. Tamura, H. Mori, Vortex shedding from two circular cylinders in staggered arrangement, J. Fluids Engine 60a (1980) 359–363.
[15] B.S. Carmo, J.R. Meneghini, Numerical investigation of the flow around two circular cylinders in tandem, J. Fluids Struct. 22 (2006) 979–988.
[16] I. Borazjani, F. Sotiropoulos, Vortex-induced vibrations of two cylinders in tandem arrangement in the proximity wake interference region, J. Fluid Mech. 621 (2009) 321–364.
[17] M.D. Griffith, D.L. Jacono, J. Sheridan, J.S. Leontini, Flow-induced vibration of two cylinders in tandem and staggered arrangements, J. Fluid Mech. 833 (2017) 98–130.
[18] G. Xu, Y. Zhou, Strouhal numbers in the wake of two inline cylinders, Exp. Fluids 37 (2004) 248–256.
[19] Y. Zhou, W. Yiu, Flow structure, momentum and heat transport in a two-tandem-cylinder wake, J. Fluid Mech. 548 (2006) 17–48.
[20] B.S. Carmo, S.J. Sherwin, P.W. Bearman, R.H.J. Willden, Flow-induced vibration of a circular cylinder subjected to wake interference at low Reynolds number, J. Fluids Engine 27 (2011) 503–522.
[21] F.J. Huera-Huarte, Z.A. Bangash, L.M. González, Multi-mode vortex and wake-induced vibrations of a flexible cylinder in tandem arrangement, J. Fluids Struct. 27 (2016) 193–211.
[22] P.R.F. Teixeira, E. Didier, Numerical simulation of flow interaction between stationaty and downstream elastically mounted cylinders in tandem at low Reynolds number, J. Braz. Soc. Mech. Sci. Eng. 39 (2017) 801–811.
[23] J. Lin, R. Jiang, Z. Chen, X. Ku, Poisseuille flow-induced vibration of two cylinders in tandem, J. Fluids Struct. 40 (7085) (2013) 70–85.
[24] X. Wu, F. Ge, Y. Hong, A review of recent studies on vortex-induced vibrations of long slender cylinders, J. Fluids Struct. 28 (2012) 292–308.
[25] R. Gautier, Calcul Haute Fidélité de la Turbulence en géométrie Complexe: Application au Contrôle Fluidique d'un Jet, Poitiers University, Poitiers, France, 2006 Ph.D. Dissertation.
[26] S. Laizet, E. Lamballais, High-order compact schemes for incompressible flows: a simple and efficient method with quasi-spectral accuracy, J. Comput. Phys. 228 (2009) 5989–6015.
[27] P. Parnaudeau, D. Heitz, E. Lamballais, J.H. Silvestrini, Combination of the immersed boundary method with compact schemes for dns of flows in complex geometry, in: Direct and Large-Eddy Simulation V, Springer, 2004, pp. 581–590.
[28] A. Bokaian, F. Geoola, Wake-induced galloping of two interfering circular cylinders, J. Fluids Mech. 146 (1984) 383–415.
[29] S. Lele, Compact finite difference schemes with spectral-like resolution, J. Comput. Phys. 103 (1992) 16–42.
[30] P. Parnaudeau, J. Carlier, D. Dominique, E. Lamballais, Experimental and numerical studies of the flow over a circular cylinder at Reynolds number 3900, Phys. Fluids 20 (2008) 085101.
[31] D. Shiels, A. Leonard, A. Roshko, Flow-induced vibration of a circular cylinder at limiting structural parameters, J. Fluids Struct. 15 (2001) 3–21.
[32] D.M.V. Vitola, Influência de um Contorno Plano Sobre o Desprendimento de Vórtices ao Redor de um Cilindro Circular, Universidade Federal do Rio Grande do Sul. Instituto de Pesquisas Hidráulicas. Programa de Pós-Graduação em Recursos Hídricos e Saneamento Ambiental, Porto Alegre, Brazil, 2006 Ph.D. Dissertation.
[33] L.C. Pinto, Análise por Simulação Numérica Direta do Escoamento ao Redor de um Cilindro Submetido a Vibração Induzida por Vórtices, Universidade Federal do Rio Grande do Sul. Instituto de Pesquisas Hidráulicas. Programa de Pós-Graduação em Recursos Hídricos e Saneamento Ambiental, Porto Alegre, Brazil, 2012 Ph.D. Dissertation.
[34] L.C. Pinto, P.S. Berwaldt, E.B. Schettini, J.H. Silvestrini, Vortex shedding around a cylinder under forced oscillation in transversal, arch and convex eight-shaped trajectories, in: Proceedings of Bluff Body Flow and Vortex Induced Vibration, BBVIV 6, Campri Island, Italy, 2010, pp. 369–372.
[35] J. Li, A. Chambarel, M. Donneaud, R. Martin, Numerical study of laminar flow past one and two circular cylinders, Comput. Fluids 19 (1991) 155–170.
[36] J. Mizushima, N. Suehiro, Instability and transition of flow past two tandem circular cylinders, Phys. Fluids 17 (2005) 104107.
[37] B. Sharman, F.S. Lien, L. Davidson, C. Norberg, Numerical predictions of low Reynolds number ows over two tandem circular cylinders, Int. J. Numer. Methods Fluids 47 (2005) 423–447.
[38] G.V. Papaioannou, D.K.P. Yue, M.S. Triantafyllou, G.E. Karnadakis, On the effect of spacing on the vortex-induced vibrations of two tandem cylinders, J. Fluids Struct. 24 (2008) 833–854.
[39] A. Mussa, P. Asinari, L. Luo, Lattice Boltzmann simulations of 2d laminar flows past two tandem cylinders, J. Comput. Phys. 228 (2009) 983–999.
[40] T. Sarpkaya, Hydrodynamic damping, flow-induced oscilations, and biharmonic response, J. Offshore Mech. Arctic Eng. 117 (1995) 232–238.
[41] M.M. Zdravkovich, Review of interference-induced oscillations in flow past two parallel circular cylinders in various arrangements, J. Wind Eng. Ind. Aerodyn. 101 (1988) 511–521.
[42] C.H.K. Williamson, Three-dimensional wake transition, J. Fluid Mech. 328 (1996) 345–407.
[43] J.S. Leontini, M.C. Thompson, K. Hourigan, Three-dimensional transition in the wake of a transversely oscillating cylinder, J. Fluid Mech. 577 (2007) 79–104.
[44] S. Mittal, V. Kumar, Flow-induced oscillations of two cylinders in tandem and staggered arrangements, J. Fluids Struct. 15 (2001) 717–736.
[45] G. Moe, Z.J. Wu, The lift force on a cylinder vibrating in a current, J. Fluids Struct. 112 (1990) 297–303.
[46] A. Khalak, C.H.K. Williamson, Fluid forces and dynamics of hydroelastic structure with very low mass and damping, J. Fluids Struct. 11 (1997) 973–982.
[47] A.E. Khalak, C.H.K. Williamson, Motions, forces and mode transitions in vortex-induced vibrations at low mass-damping, J. Fluids Struct. 10 (1999) 455–472.